

# Iron-related carrier traps near the $n^+p$ -junctions of crystalline silicon solar cells: impacts of feedstock and of the fabrication processes

Teimuraz Mchedlidze\* and Jörg Weber

Institut für Angewandte Physik, Technische Universität Dresden, 01062 Dresden, Germany

Received 24 January 2014, revised 17 June 2014, accepted 17 June 2014

Published online 10 July 2014

**Keywords** DLTS, Fe-related carrier traps, photovoltaics, pn-junctions, silicon, solar cells

\* Corresponding author: e-mail teimuraz.mchedlidze@physik.tu-dresden.de, Phone: +49 351 463 37227, Fax: +49 351 463 37060

An influence of the iron content in the crystal on the formation of carrier traps in the silicon solar cells was studied. Mesa-structured  $n^+p$ -junctions were formed on the surface of Cz-Si wafers after various stages of a standard solar cell fabrication process. Majority carrier traps in/near the junction volume were investigated by deep level transient spectroscopy (DLTS). The trap density correlated with the total iron content in the wafers and dropped strongly with the distance from the junctions. Our

results suggest that the traps were formed during the phosphorus diffusion process and/or during the subsequent cooling. The initial iron content in the wafers influenced changes in the trap concentrations at further fabrication steps. The present study could help in increasing solar cell efficiencies by tailoring the fabrication processes according to the contamination in the feedstock.

© 2014 WILEY-VCH Verlag GmbH & Co. KGaA, Weinheim

**1 Introduction** The reduction of the production costs for Si solar cells necessitates a reduction in the purity of the Si feedstock [1]. Several recent studies address the tolerable concentration levels of different contaminations in the feedstock (see Ref. [1] and references therein). Among others, iron is in the focus of such investigations due to its strong detrimental effect on the solar cell performance (see Ref. [2–4] and references therein), the high prevalence in the Si feedstock [1] and the difficulties in passivation/gettering of iron-related defects in crystalline Si [5].

Various types of iron-containing defects can co-exist in Si. In boron doped p-type Si, the base material for most Si solar cells, interstitial iron atoms ( $Fe_i$ ) are the most detrimental species [5]. Different type of defects, FeB pairs, are formed due to the Coulomb attraction of  $Fe_i^+$  and  $B^-$  species and the sufficient mobility of  $Fe_i$  atoms even at temperatures  $<100^\circ\text{C}$ . Under influence of light and/or temperature the chemical equilibrium  $FeB \leftrightarrow Fe_i + B_s$  changes and determines the actual content of  $Fe_i$  and FeB species in the bulk of Si [5]. During cooling from high temperatures iron atoms precipitate into iron silicide, due to decrease of solubility of iron in Si with decrease in temperature [1]. In addition, iron atoms interact with lattice defects (dislocations, stacking-faults, etc.) [6–8], oxide

precipitates [9], intrinsic defects [10], and other impurity atoms and complexes [5]. Despite many investigations the picture for the electrical activity of various Fe-containing defects, complexes, and precipitates in Si is far from being complete.

The Fe-containing defects can be detected and identified by several experimental techniques [5, 11]. Unfortunately, none of these methods is capable of detecting all existing Fe-containing defects with sufficient sensitivity or precision. Deep level transient spectroscopy (DLTS) is, e.g., capable to identify and to determine concentration of  $Fe_i$ , FeB, and many other Fe containing point-like complexes [5, 12]. Although a DLTS signal from iron silicide precipitates was also reported previously [13], estimation of the iron concentration from the signal intensity could not be done due to the extended character of the defects.

The electrical properties of Si wafers are influenced by the process steps for fabricating Si solar cells, e.g., dopant diffusion, coatings, electrical contact formation, etc. The properties are also strongly dependent on the starting material. A better understanding of the defect formation during the solar cell fabrication could suggest modifications of the process steps improving the solar cell efficiencies and reducing the fabrication costs at the same time. Special

investigations were performed for multi-crystalline silicon (see e.g., [14]) to determine the dominant physical mechanism controlling the electrical quality of the material during the solar cell fabrication. For crystalline Si grown by the Czochralski process (Cz-Si) a similar investigation appeared only recently [15]. However, in the both cases only defects formed in the bulk (the base) of the solar cells were investigated. The increase for the bulk carrier lifetime was observed in iron-contaminated mc-Si and/or Cz-Si solar base materials after phosphorus diffusion process followed by its relatively small deterioration after formation of electrical contacts [14, 15].

Recently, we reported on traps in the vicinity of  $n^+p$ -junctions in the Cz-Si solar cells [16]. Majority carrier traps, detrimental for the solar cell efficiency (see Ref. [17] and references therein), were formed in the vicinity of the  $n^+p$ -junctions during processing. The density of the traps steeply decreased with the distance from the junction. We will label these defects as near junction volume (NJV) defects.

In the present work, we identify the processing steps responsible for the formation of the NJV defects, discuss their possible origin, and investigate the influence of the subsequent processes on the defect concentration for Cz-Si samples with different initial iron content.

**2 Samples and experimental** Three Si single crystals (labeled A, B, and C in Ref. [15]) with elevated iron content were specially grown by the standard Cz-process at Bosch Solar Energy AG. The crystals were pulled from different Si feedstock and doped with boron to obtain a resistivity in the range of 3–6  $\Omega\text{cm}$ . Standard sized, 150  $\mu\text{m}$  thick and  $156 \times 156 \text{ mm}^2$  squared Si wafers were cut-out from the lower quarter of the Cz-Si crystals.

In Ref. [15] the  $\text{Fe}_\text{I}/\text{FeB}$  content of the as-grown A–C wafers was determined by lifetime measurements (LT) and DLTS. The total iron content was also determined by inductively-coupled plasma mass-spectroscopy (ICPMS). The difference between LT/DLTS and ICPMS results originates from the different sensitivities and selectivity of the methods. ICPMS determines the total iron concentration with a detection limit in Si of only  $\sim 3 \times 10^{13} \text{ cm}^{-3}$ . Both LT and DLTS give the concentration of  $\text{Fe}_\text{I}/\text{FeB}$  recombination centers with much better detection limits but are less sensitive to the precipitated iron.

Recently, we have developed a procedure to determine the total iron concentration in the crystalline Si samples by DLTS [18]. The procedure includes a high temperature ( $T_\text{a}$ ) anneal for a sufficient time ( $t_\text{a}$ ) followed by a fast quench to room temperature (HTAQ). During the HTA stage Fe-containing precipitates are dissolved and Fe atoms are transferred into  $\text{Fe}_\text{I}$  state. **Very fast quenching from  $T_\text{a}$  to  $T < 100^\circ\text{C}$  prevents  $\text{Fe}_\text{I}$  from formation of precipitates. Later  $\text{Fe}_\text{I}$  forms FeB pairs at room temperature. The required parameters of the HTAQ procedure for the A–C materials, i.e.,  $T_\text{a} = 950^\circ\text{C}$ ,  $t_\text{a} = 30 \text{ min}$  and the quenching time  $\sim 1 \text{ s}$ , were established in separate experiments [18].**

The concentration of FeB pairs in the HTAQ subjected samples was determined using standard DLTS measurement procedures on Schottky diodes explained below. The level of background Fe contamination of our HTAQ process was determined using a reference electronic grade FZ-grown p-type Si sample. The sample was treated in the same batch with the A–C samples intended for HTAQ process and subjected to the all HTAQ steps. The background Fe concentration level detected in this sample after HTAQ process, i.e.,  $1.2 \times 10^{12} \text{ cm}^{-3}$ , was subtracted from the FeB trap densities detected in the other quenched samples.

The wafers were subjected to the standard consecutive processing steps of a solar cell fabrication process [15, 19]. These steps can be grouped in four stages. The first, cleaning stage (C) includes: saw damage removal by KOH without texturization and RCA cleaning. The second, phosphorus diffusion stage (P) includes: phosphorus silicate glass (PSG) deposition, phosphorus diffusion, PSG removal and cleaning. The antireflection (AR) coating is fabricated at the third stage: deposition of the AR coating ( $\text{Si}_3\text{N}_4$  film) followed by appropriate tempering treatment. The last stage (E) is formation of electrical contacts: screen printing of Ag and Al paste, solvent evaporation, and sintering of the electrical contacts. All processing steps for our samples were performed at CIS (Erfurt, Germany). Further details and parameters, i.e., temperatures, durations, etc., of the applied solar cell process are given in Ref. [15]. Hereinafter in the labels of the samples a letter specifying starting material will be followed by a letter specifying the last applied processing stage (see Table 1). Note, that letter Q in the table stands for the HTAQ procedure.

For the measurements we used samples,  $10 \times 5 \times 0.15 \text{ mm}^3$  in size, cut-out at the  $\sim 45 \text{ mm}$  distance from the center of the A–C wafers. The #Q samples for determination of total Fe concentrations and the #C samples were cut-out from the neighbor locations. For DLTS measurements, the #Q and #C samples were etched in  $\text{HF} + \text{HNO}_3$  (1:5) solution for 1 min. Subsequently, 50 nm thick Al dots with  $1 \text{ mm}^2$  area were evaporated on the surface of the samples for the Schottky contacts. Ohmic contacts were formed by rubbing-in InGa eutectic solution to the reverse surface of the samples.

**Table 1** Iron concentration in the samples measured after HTAQ treatments and labels of the samples subjected to various treatments and/or fabrication processes.

sample	A	B	C
$C_\text{Fe}$ ( $10^{12} \text{ cm}^{-3}$ )	$44 \pm 6$	$2.7 \pm 0.4$	$7.1 \pm 0.4$
process	sample labels <sup>a</sup>		
C	AC	BC	CC
C + HTAQ	AQ	BQ	CQ
C + P	AP	BP	CP
C + P + AR	AAR	BAR	CAR
C + P + AR + E	AE	BE	CE

<sup>a</sup>“#” in the label will be used as a wildcard.

Wafers taken from the sister locations of the crystals were subjected to P, AR, and E fabrication stages. Samples cut-out from the wafers at similar locations were used in the DLTS measurements. Mesa-diodes were formed on top of the #P, #AR, and #E samples.

The room temperature preparation of mesa-diodes out of the n<sup>+</sup>p-junction of the solar cell after the E stage was already described in a previous publication [16]. For the samples after P and AR stages, we first removed the oxide and nitride layers from the front surface of the samples by etching in HF + H<sub>2</sub>O (1:5) solution for 3 min. at room temperature. Then a 50-nm Al layer was deposited on the P-doped surface. Subsequently, the mesa structures were fabricated using the similar procedures as described in Ref. [16]. Finally, Ohmic contacts for the #P and #AR samples were formed by rubbing-in InGa eutectic solution onto the back surfaces. For the #E samples the back Al contact of the solar cell was used as the Ohmic contact.

In parallel, the bulk of the #P, #AR, and #E samples was also analyzed. For this, the samples were cut-out from the neighbor positions to those used in the mesa-diode measurements. The n<sup>+</sup>p-junction structures was completely removed by etching away ~50 μm of material from the surface of the samples. The standard Schottky diodes were fabricated on the top of the etched samples.

DLTS measurements were performed by means of a standard lock-in system working at the capacitance test frequency of 1 MHz. Principles of the method and the system were previously described [20]. Sample temperature could be varied in the range from 35 to 300 K.

**3 Results and discussion** The levels of FeB concentration in the #Q samples after the HTAQ procedure and after subtraction of the Fe background signal are presented in Table 1. These FeB concentrations agree with those of the ICPMS measurements [15]. In addition, several traps in concentration ~3–5 × 10<sup>11</sup> cm<sup>-3</sup> were also detected in #Q samples. The parameters of these traps were same as reported in Ref. [18] for the similar samples. With densities much smaller than those for the FeB pairs, these traps were out of the focus of the present study.

The DLTS spectra of #P samples are presented in Fig. 1. The spectra were detected at the depth  $d \sim 0.8 \mu\text{m}$  below the (metallurgical) junction of the n<sup>+</sup>p-diode. Besides the previously reported **TM1 peak** [16], two additional peaks overlapping with the TM1 can be identified in sample AP. The lower temperature peak was attributed to the **FeD** trap reported in Ref. [10], due to the similarity of the trap parameters ( $E_{\text{H175}} = E_{\text{v}} + 0.33 \text{ eV}$ ,  $\sigma_{\text{H205}} \approx 3.2 \times 10^{-15} \text{ cm}^2$ ). The parameters for the high temperature peak (H235 in Fig. 1) were difficult to determine due to the small intensity and the overlap with the TM1 peak. Sample AP showed a large variation of NJV defects and their concentrations with the spatial location of the mesa-diode on the sample surface. The intensity of the peaks strongly decreased with the distance from the junction  $d$  and for values of  $d > 1.5 \mu\text{m}$  usually only the TM1 peak remained in the spectra. The

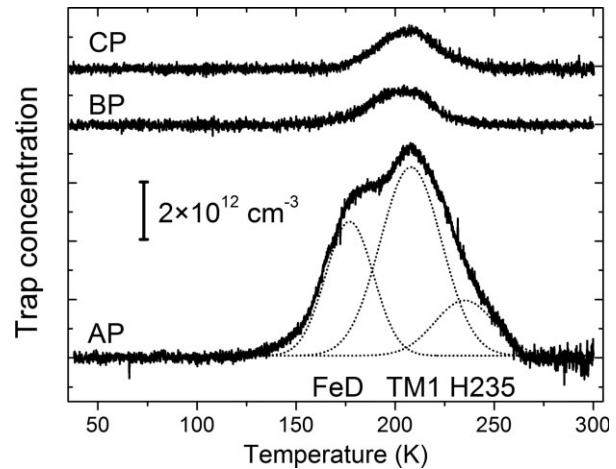


**Figure 1** DLTS spectra detected at a depth  $d \sim 0.8 \mu\text{m}$  from the n<sup>+</sup>p-junction of samples AP–CP. The scale for the trap concentration is indicated. Spectra are shifted vertically for clarity. Decomposition of the spectrum into individual peaks is presented for the AP sample by dotted lines. Parameters of the DLTS measurements are: reverse bias  $U_{\text{R}} = 2 \text{ V}$ , pulse bias  $U_{\text{P}} = 0.01 \text{ V}$ , sampling time  $t_{\text{W}} = 48 \text{ ms}$ , and pulse duration  $t_{\text{P}} = 0.25 \text{ ms}$ .

additional traps formed in the NJV of the AP sample deserve separate investigation and are out of the scope of the present report. Below, we will consider only data related to the TM1 traps, since only these traps were detected in all samples at various fabrication stages.

Spectra detected in samples A# at the depth of  $d \approx 1.5 \mu\text{m}$  from the junction, after different processing stages are presented in Fig. 2. The spectrum AC detected

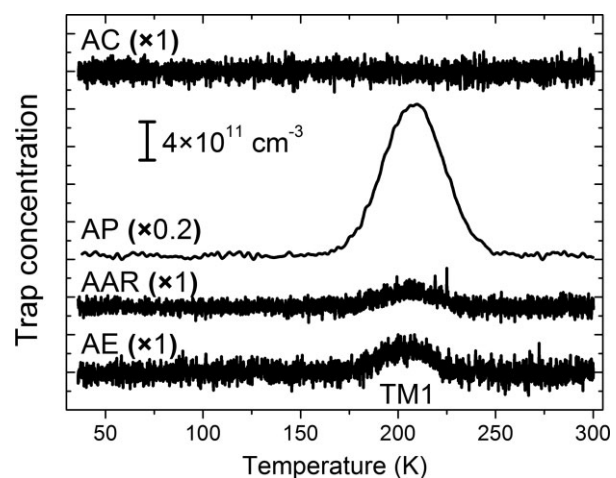


**Figure 2** DLTS spectra after various fabrication stages detected in A# samples at a depth of  $d \approx 1.5 \mu\text{m}$  from the n<sup>+</sup>p-junction. Attributions, magnification factors and the scale for the trap concentration are indicated. Spectra are shifted vertically for clarity. Parameters of the DLTS measurements are: reverse bias  $U_{\text{R}} = 5 \text{ V}$ , pulse bias  $U_{\text{P}} = 1 \text{ V}$ , sampling time  $t_{\text{W}} = 48 \text{ ms}$ , and pulse duration  $t_{\text{P}} = 0.25 \text{ ms}$ .

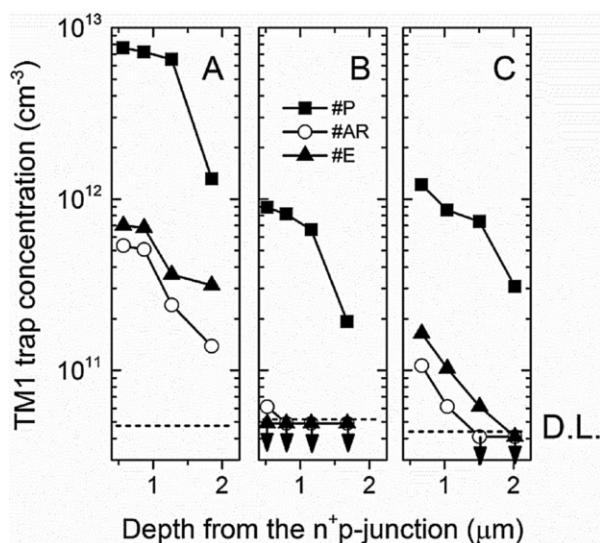


**Figure 3** The concentration profiles for the TM1 signal in samples A#–C#. Dotted line presents the detection limit (D.L.) for trap densities in each sample. The experimental points are connected to guide the eye. Arrows beneath to the data points signify that the values were UDL.

from a Schottky diode fabricated before processing of the wafer is also included in the figure for comparison. In Fig. 2 the TM1 concentration drops substantially after the formation of anti-reflection coating. However, the subsequent sintering of electrical contacts leads to an increase of the TM1 concentration again. It should be stressed, that for all the samples with etched-off junctions the DLTS signals detected in the mesa-diodes were under the detection limits.

The concentration profiles, i.e., the dependence of the TM1 peak intensities in samples A#–C# on the depth from the  $n^+$ p-junction are presented in Fig. 3. The results detected after three subsequent solar cell process stages are presented (#P, #AR, and #E). Note the slightly different DLTS signal detection limits (D.L.) for samples A–C related to the different doping levels for the samples. From the profiles in Fig. 3 it seems obvious that after the each stage the NJV trap concentration is the largest for sample A and the smallest for sample B, in accordance with the total Fe concentration determined after HATQ. For samples A# and C# a substantial decrease in the defect concentration after the AR stage is followed by a noticeable increase initiated by the E stage. Such an increase was not detectable in the case of the sample B#.

An integration of the depth profiles provides an estimate for the total number of the NJV traps (i.e., area density). Figure 4 compares the TM1 area density near the junction with the total Fe concentration in the unprocessed wafer. For sample B after the full fabrication process (BE) only an upper limit of the NJV-concentration was estimated from the DLTS signal detection limit. Figure 4 suggests a direct relationship of the TM1 density with the Fe concentration in the crystals. Moreover, the slope obtained from fitting the

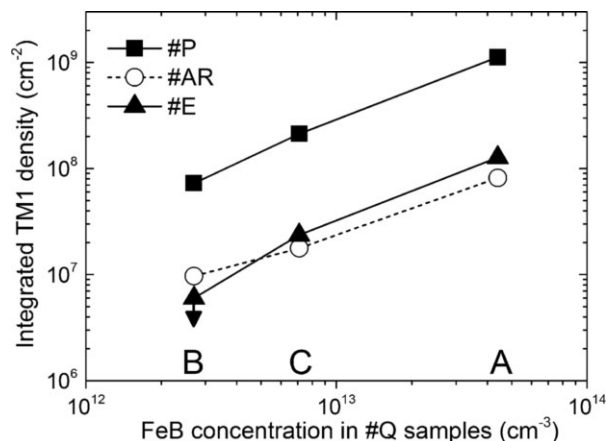


**Figure 4** Correlation between FeB concentrations in the AQ–CQ samples and the integrated TM1 area density after the PV fabrication stages. The experimental points are connected to guide the eye.

experimental points for each process stage is very close to unity ( $0.97 \pm 0.04$ ), indicating that the defects responsible for TM1 most probably contains a single Fe atom. Previously we reported [16] that two traps with close parameters (TM1.1:  $E_t = E_v + 0.37$  eV,  $\sigma = 3.1 \times 10^{-16}$  cm<sup>2</sup> and TM1.2:  $E_t = E_v + 0.42$  eV,  $\sigma = 1 \times 10^{-15}$  cm<sup>2</sup>) were found responsible for the dominant TM1 peak detected in the spectrum of the  $n^+$ p-junction. Unfortunately, during the present study it was not possible to follow changes in the intensities of TM1.1 and TM1.2 signals separately due to their small intensities.

For further discussion on origins for the NJV traps let us summarize the results reported in Ref. [16] and combine them with those from the present study. It was reported in Ref. [16] that both TM1.1 and TM1.2 trap densities steeply decreased with distance from the  $n^+$ p-junction, the traps were neutral before thermal excitation and the both signals originated from point-like defects. It was also noticed that the parameters of TM1.2 trap well match those reported for the interstitial Fe-atom in Si [5], while TM1.1 can be attributed to FeP (FeVP) complex. The present results suggest that traps were formed after phosphorus diffusion and their density well correlated with total iron content in the material.

A consistent mechanism of the trap formation can be formulated as follows. In the as-cut wafers most of the iron atoms were contained in iron-silicide precipitates [21]. Heating the samples during the P-diffusion process initiated partial dissolution of the precipitates. Due to the gettering of iron in the P-diffused layer there exists a flow of iron atoms from the bulk. On the other hand, the P-diffusion process involves injection of various defects and complexes to the NJV [22]. Fast cooling after finish of the diffusion process causes interaction of Fe atoms with the injected species and formation of the detected traps. This mechanism is well consistent with the observed density profiles for the traps



resembling the diffusion profile itself. Formation of FeP (FeVP) complexes well fits the proposed mechanism as well. Detection of the FeD trap in AP sample, which was identified as a donor state of iron-vacancy pair [10], also supports the mechanism described. However, presence of Fe<sub>i</sub> with the steep intensity profile for such a mechanism is puzzling. Moreover, in p-type Si, one would expect interaction of Fe<sub>i</sub><sup>+</sup> with B<sup>-</sup> and formation of FeB pairs. Therefore, we suppose that the defect responsible for the TM1.2 is not Fe<sub>i</sub>, but some complex involving Fe atom and intrinsic defects and/or phosphorus. The close coincidence of the trap parameters with those for the Fe<sub>i</sub> is not a unique phenomenon for Fe-containing defects. For example, the trap parameters well coincides for Fe<sub>i</sub> and for small Fe precipitates (Fe<sub>4</sub>), as it was reported in Ref. [23]. Only different response of the signals on the filling pulse length due to extended character of the precipitates allowed separation of the two signals in Ref. [23]. In the present case TM1.2 reveals a point-like defect behavior similar to that of Fe<sub>i</sub>, complicating their distinction attempts.

One should also keep in mind that in the sample AP, with the highest initial Fe content, the variety and concentrations of traps after the P-diffusion was the largest. This suggests that iron atoms in NJV actively participate in defect formation processes. It can be supposed that for high iron concentrations the defects containing several iron atoms together with interstitial defects and/or phosphorus could be formed. The origin of the TM1 related traps definitely deserves further investigation in the future.

The efficiency of the P-diffusion for the iron-gettering depends on the size and density of the precipitates present in the material before the start of the P-diffusion process and also on the process parameters [21]. Several scenarios could be visualized, where the final result will be related to the state of precipitate dissolution, the speed of the gettering process and the speed of back-precipitation: iron silicide precipitates, which were not fully dissolved during the P-diffusion process could also form sinks for the dissolved iron atoms during cooling. As a result, one may even imagine a scenario where cleaner starting material after the processing leads to a smaller final bulk carrier lifetime due to the larger resulting density of Fe<sub>i</sub>/FeB traps. First observations of such a situation were recently reported for the case of iron contaminated crystalline solar cells with implanted emitters [24].

The AR stage led to a suppression of the TM1 trap density by one order of magnitude. Note, that the decrease is larger for the samples AAR and CAR. This may be related to iron-containing precipitates remaining after the P-diffusion process in those samples. These precipitates could serve as an additional sink for Fe atoms, which were freed from the dissociated TM1 traps by the mechanism considered in Ref. [24]. Another possibility for the AR process influence may be a passivation of the TM1 defects by hydrogen indiffused from the deposited SiN<sub>x</sub>:H layer (by analogy to, e.g., [25]). We were not able to detect formation of any H-related traps after AR process by DLTS.

The contact sintering stage E comprises a fast thermal treatment at high temperature (800 °C, see, e.g., [15, 19]). This process can again initiate partial dissolution of the remaining Fe-precipitates [26, 27], leading to the additional formation of the TM1 traps. Such a behavior could explain the increase of the TM1 trap density after the E stage for samples AE and CE. In sample BE an increase in TM1 concentration after the E stage was not observed (see Fig. 4). This suggests that for the material of B sample the P-diffusion process caused full dissolution of the iron-containing precipitates in the bulk and a nearly complete gettering of the Fe atoms to the P-diffused layer as a result of the complete solar cell process. All the results indicate a tolerable Fe concentration in Cz-Si crystals for our PV-process of  $C_{\text{Fe}} = C_{\text{crit}} \leq 3 \times 10^{12} \text{ cm}^{-3}$ .

Interestingly, in Ref. [28] the authors suggested that iron concentrations below  $C_{\text{Fe}} = 10^{12} \text{ cm}^{-3}$  will not affect the efficiency of the cells, in full agreement with the value obtained in the present work. Moreover, in Ref. [29] a significant deterioration of the cell efficiencies was reported above a contamination level of  $C_{\text{Fe}} = 10^{12} \text{ cm}^{-3}$  for the standard cell fabrication processes. The results suggest that formation of NJV traps seriously affects the solar cell efficiency. In addition, in Ref. [29] it was proposed that the efficiency of the cells fabricated using Si material containing high concentrations of iron may be substantially improved by applying modified phosphorus gettering processes. We suggest that proper process parameters could be selected by monitoring the behavior of the NJV defects.

**4 Summary** Majority carrier traps were detected by DLTS in the near-to n<sup>+</sup>p-junction volume (NJV) of Si solar cells. The influence of different solar cell processes was studied and a direct relation of the defect concentration to the Fe content in the crystals was shown. The density of the traps was highest after the P-diffusion process. The formation of the anti-reflection coating suppressed the Fe-related NJV trap density. However, in samples with Fe content above critical level, additional NJV defects were created after the contact sintering. For the standard PV process, used in this study, we deduce a tolerable iron concentration of  $C_{\text{crit}} \leq 3 \times 10^{12} \text{ cm}^{-3}$ .

Our results indicate a way to control the parameters of a solar cell fabrication process, which could lead to a careful tailoring of the process parameters to the Fe content in the crystal. Such a tuning of the processing steps could allow even higher tolerable Fe concentrations for the feedstock.

**Acknowledgements** The authors would like to thank the colleagues from Bosch Solar Energy AG and CIS (Erfurt, Germany) for growing the crystals, the preparation of wafers and for performing the solar cell fabrication processes. The work was supported by the German Ministry for Education and Research under contract 03SF0398K (xμ-Material) in the framework of the Excellence Cluster Solar Valley Central Germany.

## References

- [1] J. Hofstetter, J. F. Lelièvre, C. del Canizo, and A. Luque, *Mater. Sci. Eng. B* **159–160**, 299 (2009).
- [2] G. Coletti, R. Kvande, V. D. Mihailetschi, L. J. Geerligs, L. Arnberg, and E. J. Øvrelid, *J. Appl. Phys.* **104**, 104913 (2008).
- [3] R. Kvande, L. J. Geerligs, G. Coletti, L. Arnberg, M. Di Sabatino, E. J. Øvrelid, and C. C. Swanson, *J. Appl. Phys.* **104**, 064905 (2008).
- [4] I. E. Reis, S. Riepe, W. Koch, J. Bauer, S. Beljakowa, O. Breitenstein, H. Habenicht, D. Kreßner-Kiel, G. Pensl, J. Schön, and W. Seifert, in: *Proc. 24th European Photovoltaic Solar Energy Conference*, edited by W. Sinke, H. Ossenbrink, and P. Helm (Hamburg, Germany, 2009), pp.2144–2148.
- [5] A. A. Istratov, H. Hieslmair, and E. R. Weber, *Appl. Phys. A* **69**, 13 (1999).
- [6] K. Sumino, *J. Phys. (France) C* **4(44)**, 195 (1983).
- [7] K. Lauer, M. Herms, A. Grochocki, and J. Bollmann, *Solid State Phenom.* **178–179**, 211 (2011).
- [8] B. Shen, X. Y. Zhang, K. Yang, P. Chen, R. Zhang, Y. Shi, Y. D. Zheng, T. Sekiguchi, and K. Sumino, *Appl. Phys. Lett.* **70**, 1876 (1997).
- [9] J. Jablonski, B. Shen, T. R. Mchedlidze, M. Imai, and K. Sumino, *Mater. Sci. Forum* **196–201**, 1859 (1995).
- [10] D. Abdelbarey, V. Kveder, W. Schröter, and M. Seibt, *J. Appl. Phys.* **108**, 043519 (2010).
- [11] A. A. Istratov, H. Hieslmair, O. F. Vyvenko, E. R. Weber, and R. Schindler, *Sol. Energy Mater. Sol. Cells* **72**, 441 (2002).
- [12] G. W. Ludwig and H. H. Woodbury, in: *Solid State Physics*, edited by F. Seitz and D. Turnbull (Academic, New York, 1962), p. 223.
- [13] M. Seibt, R. Khalil, V. V. Kveder, and W. Schröter, *Appl. Phys. A* **96**, 235–253 (2009).
- [14] A. Cuevas, and D. MacDonald, *Multicrystalline Silicon: A Review of its Electronic Properties*, PVSEC 2005 (Shanghai Scientific & Technological Literature Publishing House, Shanghai, 2005), pp. 521–524.
- [15] K. Lauer, C. Möller, K. Neckermann, M. Blech, M. Herms, T. Mchedlidze, J. Weber, and S. Meyer, *Energy Proc.* **38**, 589 (2013).
- [16] T. Mchedlidze, L. Scheffler, J. Weber, M. Herms, J. Neusel, V. Osinniy, C. Möller, and K. Lauer, *Appl. Phys. Lett.* **103**, 013901 (2013).
- [17] Zh. S. Karazhanov, *Appl. Phys. Lett.* **76**, 2689 (2000).
- [18] T. Mchedlidze and J. Weber, *Phys. Status Solidi RRL* **8**, 228 (2014).
- [19] J. Szlufcik, F. Duerinckx, E. van Kerschaver, R. Einhaus, A. Ziebakowski, E. Vazsonyi, K. D. Clercq, J. Horzel, L. Frisson, J. Nijs, and R. Mertens, in: *Proc. 14th European Photovoltaic Solar Energy Conference*, edited by H. A. Ossenbrink, P. Helm, and H. Ehmann (WIP-Munich, Germany, 1997), p. 380.
- [20] G. L. Miller, D. V. Lang, and L. C. Kimerling, *Annu. Rev. Mater. Sci.* **7**, 377 (1977).
- [21] J. Hofstetter, D. P. Fenning, J.-F. Lelievre, C. delCanizo, and T. Buonassisi, *Phys. Status Solidi A* **209**, 1861 (2012).
- [22] A. Bentzen, A. Holt, J. S. Christensen, and B. G. Svensson, *J. Appl. Phys.* **99**, 064502 (2006).
- [23] R. Khalil, V. Kveder, W. Schröter, and M. Seibt, *Phys. Status Solidi C* **2**, 1802 (2005).
- [24] V. Vähänissi, A. Haarahiltunen, M. Yli-Koski, and H. Savin, *IEEE J. Photovoltaics* **4**, 142 (2014).
- [25] P. Karzel, A. Frey, S. Fritz, and G. Hahn, *J. Appl. Phys.* **113**, 114903 (2013).
- [26] J.-F. Lelièvre, J. Hofstetter, A. Peral, I. Hoces, F. Recart, and C. del Cañizo, *Energy Proc.* **8**, 257 (2011).
- [27] B. Michl, J. Schön, F. Schindler, W. Warta, and M. C. Schubert, in: *Proc. 27th European Photovoltaic Solar Energy Conference*, edited by S. Nowak, A. Jäger-Waldau, and P. Helm (Frankfurt, Germany, 2012), pp.709–713.
- [28] S. Dubois, O. Palais, M. Pasquinelli, S. Martinuzzi, C. Jaussaud, and N. Rondel, *J. Appl. Phys.* **100**, 024510 (2006).
- [29] V. Vähänissi, A. Haarahiltunen, H. Talvitie, M. Yli-Koski, and H. Savin, *Prog. Photovolt.: Res. Appl.* **21**, 1127 (2013).